



**POLITECNICO
DI TORINO**



**Université
de Paris**

Master's double degree in Nanotechnologies for ICTs and Quantum Devices

Master Thesis

**InGaAs/GaAsSb Type-II
Superlattice for infrared imaging
towards $2.5 \mu m$**

Supervisors

Prof. Carlo Ricciardi

Prof. Maria Luisa Della Rocca

Candidate

Marco Benfante

Supervisor

III-V Lab

Dr. Jean-Luc Reverchon

July 2020

Abstract

In the frame of the European SWIRup project, this work deals with the research of new materials for the detection of the upper band of Short Wavelength InfraRed (SWIR) radiation up to $2.5 \mu m$ at high working temperature. The current technology, consisting of HgCdTe, shows some limitations and it requires cryogenic temperatures to work. As alternative, InGaAs/GaAsSb Type-II SuperLattice (T2SL) is analysed through $\mathbf{k}\cdot\mathbf{p}$ simulations. From experimental Quantum Efficiency (QE) measurements on some test devices, the problem of carrier localization appears as an exponential dependence on temperature of the QE at a given wavelength. By means of the simulations, the structure is optimized by following a quite simple model based on the scattering time. In particular, strain in the superlattice layers is adopted to achieve the lowest effective mass at the highest cutoff wavelength.

Acknowledgements

First, I would like to thank the III-V Lab that has given me the opportunity to practice on real applications of physics through its facilities. I would like then to thank all the group I worked with and in particular Dr. Jean-Luc Reverchon who personally followed me throughout all my internship. Being forced from the COVID19 to telework, I always received support from him. My second thought goes to Dr Virginie Trinité who managed to make me work on all the simulations by sending her personal computer to my apartment through courier. For the scientific discussions, besides Dr. Reverchon, I would like to thank Dr. Borge Vinter and Dr. Axel Evirgen. With the first I had conversations about the theoretical model used in the simulations while with the latter I had discussions about experimental sides concerning the growth of superlattices and direct feedbacks on the feasibility of simulated structures.

I would like also to thank my university Politecnico di Torino that gave me a really valid scientific education and Université de Paris that opened me this opportunity.

Besides the academic environment, I would like to thank my friends and colleagues for the reciprocal support during the whole year.

My most important thought goes to my parents who have always believed in me giving me the strength to go on.

Contents

List of Tables	III
List of Figures	IV
1 Introduction	1
2 Heterostructures	4
2.1 The resonant-tunneling diode	4
2.2 Superlattices: does (mini)band transport always occur?	6
2.3 Type-II superlattices and device's structure	8
3 Results	11
3.1 Experimental quantum efficiency spectra	11
3.2 Localization analysis through kp simulations	12
3.2.1 Introduction of strain	15
4 Conclusions	21
Appendices	22
A kp model	23
A.1 Bulk	23
A.2 Superlattice	25

List of Tables

1.1	Infrared spectrum ranges.	1
3.1	Tested SWIRUP T2SL at III-V lab	12
3.2	Band properties of tested devices	13
3.3	Biaxial strain in percentage for $In_xGa_{1-x}As$ in extension and $GaAs_ySb_{1-y}$ in compression	18
3.4	Simulated devices with GaAsSb in compression	18
3.5	Biaxial strain in percentage for $In_xGa_{1-x}As$ in compression and $GaAs_ySb_{1-y}$ in extension	19
A.1	Character table of the double group of the point Γ in zinc-blende-type semiconductors.	24
A.2	$ j, m_j\rangle$ valence band states in zinc-blend crystals.	25

List of Figures

2.1	Types of heterostructure and double barrier resonant tunneling	5
2.2	Resonant tunneling diode characteristic	5
2.3	Transmission for a finite superlattice	6
2.4	Kronig-Penney simulated bandwidth of (10,10) $In_{0.53}Ga_{0.47}As/GaAs_{0.51}Sb_{0.49}$ superlattice	7
2.5	SWIRup photodiode structure	9
2.6	T2SL absorption: direct and reciprocal space	10
2.7	Valence bands anticrossing in quantum wells	10
3.1	Quantum Efficiency for ART3993, ART4013 and ART4015 devices	12
3.2	Band diagram and band structure for device ART4013	13
3.3	Cutoff wavelength, band edge effective mass, C_{B1} and V_{B1} , $V_{B1} - V_{B2}$ trends for $In_{0.53}Ga_{0.47}As/GaAs_{0.51}Sb_{0.49}$ T2SL	14
3.4	Energy gap as a function of the lattice constant for several binaries with interpolating lines for the corresponding ternaries	15
3.5	Effect of biaxial strain in GaAsSb band structure	16
3.6	GaAsSb in compression: some useful trends	17
3.7	Effect of strain on the band edges of InGaAs and GaAsSb compared to the unstrained case.	18
3.8	Effective mass and zone-center HH-LH splitting as a function of cutoff wavelength	19
3.9	Effect of strain on the band edges of InGaAs and GaAsSb compared to the unstrained case.	20
3.10	Type-I transition for heavy hole in strain-compensated T2SL with GaAsSb in extension	20
A.1	III-V semiconductor's valence bands.	25
A.2	18×18 $\mathbf{k} \cdot \mathbf{p}$ model.	26

Chapter 1

Introduction

InfraRed (IR) is an ElectroMagnetic (EM) radiation whose wavelength sweeps from $0.75 \mu m$ up to $100 \mu m$. Applications using such wavelengths regard for example gas sensing, sample composition analysis and environmental control. This is because many chemical compounds such as Carbon Dioxide (CO_2) have absorption lines located in this range.

The IR spectrum can be divided into several ranges according to the wavelength (table 1.1).

Division name	Wavelength (μm)
Near InfraRed (NIR)	0.75 - 1
Short Wavelength InfraRed (SWIR)	1 - 2.5
Mid Wavelength InfraRed (MWIR)	3 - 5
Long Wavelength InfraRed (LWIR)	8 - 12
Far InfraRed	15 - 100

Table 1.1: Infrared spectrum ranges.

The focus of this work is on the SWIR range in the frame of the SWIRup project. SWIRup is a European Commission H2020 project aimed at image sensors for high-resolution earth observation missions in the upper band of shortwave infrared (up to $2.5 \mu m$) and more specifically for atmospheric gas analysis and hyperspectral imaging. The main idea is to replace Mercury Cadmium Telluride (HgCdTe) which is today the predominant material system used in SWIR applications. This is because HgCdTe material system often suffers from poor material uniformity, difficult material growth, device instability, high cost, low yield and it needs to work at cryogenic temperatures[1].

In the SWIR range, bulk InGaAs on InP works quite well up to $1.7 \mu m$ with low dark current and high quantum efficiency (about 70%). However, in order to extend the detection wavelength, the In content has to be increased leading to higher strain and high defect percentage which lowers the quantum efficiency and increases the dark current[2]. Another solution may be bulk InGaAsSb on InP or GaSb substrate. The first can reach a maximum cutoff wavelength of $1.8 \mu m$; the second is in principle adequate since it has a cutoff tunability between $1.6 \mu m$ and $2.5 \mu m$ nevertheless the technology is not mature yet. In this context, Type-II superlattices (T2SL) have gained significant interest in recent years as an important infrared material system for high-performance detectors reaching cutoff

wavelengths up to $30\ \mu\text{m}$ [2]. T2SL is a minority carrier device with type-II band alignment. In its unique structure, based on alternating thin nano-layers, the absorption of a photon induces a diagonal transition in which the electron and the hole are spatially separated in two different adjacent layers. The transition occurs close to the interface between the two layers where the two wavefunctions overlap. Since the conduction and valence bands reside in different materials, the T2SL gap results lower than that of each of the components, effectively creating an artificial bandgap. The diagonal generation of carrier has, in this case, an intrinsic drawback that derives from the reduced oscillator strength and therefore absorption with respect to bulk absorbers[3].

The main advantage of T2SL is the capability to tailor the gap playing with materials, layers' thickness and composition. Other characteristics are the stronger immunity to tunneling and the reduced Auger recombination with respect to bulk detectors[4]. III-V semiconductors, grown on GaSb or InP substrates, are appropriate to make T2SL detectors in each of the IR ranges. For the MWIR and LWIR ranges, InAs/InAsSb T2SL on GaSb Focal Plane Array (FPA) have been demonstrated[5]. InAs/GaSb T2SL has a wider gap tunability from SWIR and can achieve the same LWIR cutoff wavelengths as the InAs/InAsSb T2SL but with shorter periods (hence better absorption strength). The problem is the very large effective mass of hole along the growth direction which reduces the diffusion of the minority carriers lowering the collection quantum efficiency. As a new candidate for the detection in SWIR, InGaAs/GaAsSb T2SL on InP have been studied[1][2][5] in these years starting from Sai-Halasz et al.[6] who first proposed this kind of structure. Recently, a quantum efficiency of $\sim 40\%$ has been measured at $2.18\ \mu\text{m}$ near room temperature[3]. In 2019, an InGaAs/GaAsSb multi-quantum wells High-speed Uni-Travelling Carrier Photodiode (UTC-PD) at $2\ \mu\text{m}$ has been also demonstrated[7].

The concrete application of these materials is made possible by the advanced fabrication techniques available nowadays (e.g. MBE, MOCVD) which ensure the production of very high-quality samples.

In this work InGaAs/GaAsSb T2SL on InP is studied as an alternative to bulk InGaAs to reach bandgap tunability up to $2.5\ \mu\text{m}$. The problem of the low and temperature-dependent quantum efficiency arising from experimental measurements at the lab is addressed. In particular, it is believed that the cause of this behaviour is the localization of holes in the GaAsSb layer. In this respect, carrier transport mechanisms in superlattices are analysed and particular attention is given to the transport properties in the case of localization. Through $\mathbf{k}\cdot\mathbf{p}$ simulations, the structure is consequently optimized in terms of effective mass lowering and band gap red-shifting towards $2.5\ \mu\text{m}$ in order to favour miniband transport. Trends in band structure properties are analysed as a function of the layer thicknesses and compositions. The latter property ultimately defines the strain with respect to the InP lattice constant and this will be the key to optimize the device.

The report is organized as follows. In the next chapter, some theoretical basics on heterostructures and carrier transport in superlattices are given. This discussion, which starts with some generalities and gives a baseline to understand superlattices, is aimed to give a model able to explain the problem of carrier localization and to guide towards the simulation results that will be presented after a description of the main characteristics of a T2SL. As last section there are the conclusions and some perspectives. An appendix on the adopted $\mathbf{k}\cdot\mathbf{p}$ model is also present at the end of the document.

The Lab and the group

This work has been carried on in III-V Lab under Thales. III-V Lab is a private R&D organisation jointly established by Nokia, Thales and the CEA whose mission is to perform research and development on III-V semiconductor components from basic research to technology transfer for industrialisation. The group I worked with and I'm still working with is lead by Dr. Jean-Luc Reverchon and it is made up of 9 people. The interests are about photodetection in the Short Wavelength and Mid InfraRed ranges both in the fundamental physics and the technological aspects. For such task, both interband and intraband processes are exploited. An example of the first is given by this work, where T2SL are investigated. For the second, Quantum Cascade Detectors (QCD) studies are mainly lead by Dr. Alexandre Delga. As stems from this work, current interests goes towards IR imagers for space applications.

Observation

I'd like to remark that in fact all the work I did was somehow influenced by the unusual starting of 2020 with the pandemic situation due to the COVID19 that forced me to work at home, physically far from the lab and from all my colleagues of the group. In this respect, all the work focused on the simulation part with the impossibility to make complementary experimental measurements in addition to the ones already performed by the group at the time of my arrival. Hopefully, some new experimental measurements may be performed during the summer.

Chapter 2

Heterostructures

2.1 The resonant-tunneling diode

An *heterostructure* is a semiconductor composed of more than one material. The junction between two different materials is called heterojunction, and this is the region where the properties of the two materials meet each other. The energy *band diagram* is typically used to display properties of heterostructures. It is a plot of the allowed electron energy states in a material as a function of position along a preselected direction. In its simplest form, the diagram contains only two lines: the bottom of the conduction band and the top of the valence band. In the case of this work, these edge states occur in the Γ k-point of the Brillouin zone of the corresponding materials and therefore the difference between these two lines corresponds to their direct gaps. In the effective mass approximation, these edges correspond to the potential energy of the corresponding carrier (hole for valence band, electron for conduction band). In the case of abrupt interfaces and undoped materials, the potential energy varies step-likely as a function of the growth direction. Remember also that usually band-edges are the zones where the density of states is higher and therefore such states determine most of the electronic properties of the system.

Depending on the band alignment, several types of heterostructure may occur (fig.2.1a).

According to these diagrams, carriers experience potential barriers and therefore general problems of quantum physics related to waves and barriers apply.

The starting point of superlattices was the discovery of *resonant tunneling* through a double potential barrier first predicted by Tsu and Esaki in 1973 [10] and then demonstrated in 1974 by Esaki, Chang and Tsu [11]. A schematic of the structure is in fig.2.1b. Negative Differential Resistance (NDR) can be observed from I(V) curves of these kind of devices (fig.2.2). The conditions to be fulfilled in order for NDR to occur are: 1) energy resonance between the energy of the electron in the emitter and the discrete level of the well and 2) lateral momentum conservation. The above NDR effect is accompanied by a resonant enhancement of the transmission. In fact, when the energy of the incoming electron matches one of the quantized levels in the well material, the wavefunction builds up within the well similar to a Fabry-Perot resonator leading to (ideally) unity transmission although the tunnelling probability through the single barriers is much lower than unity (fig.2.3, lowest curve). **Scattering mechanisms** however may destroy the coherence of the process preventing the *Fabry-Perot effect* and therefore the resonant enhancement of

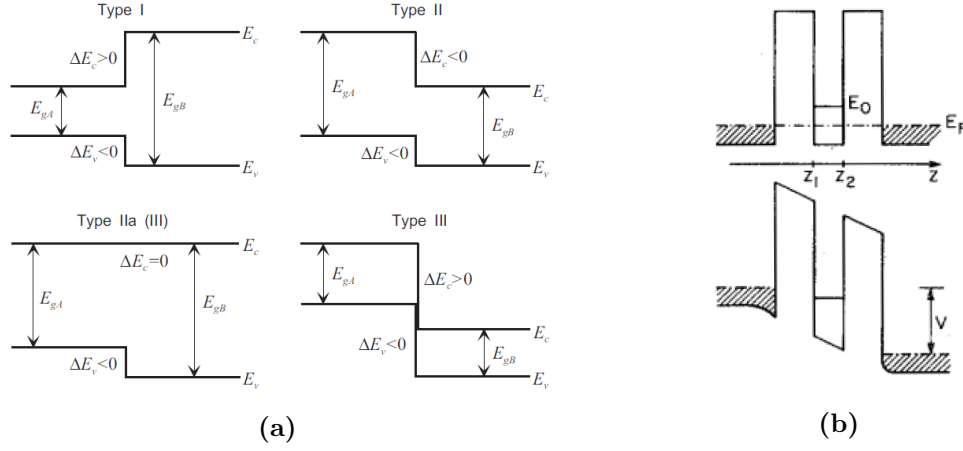


Figure 2.1: (a) Types of heterostructure from [8] and (b) Double barrier structure with degenerate-doped emitter and collector at equilibrium and with applied voltage. When the proper voltage is applied, resonance occurs and NDR is observed in the $I(V)$ characteristic. From [9].

the transmission. In the latter case, tunnelling must be viewed as an incoherent (sequential) process [9].

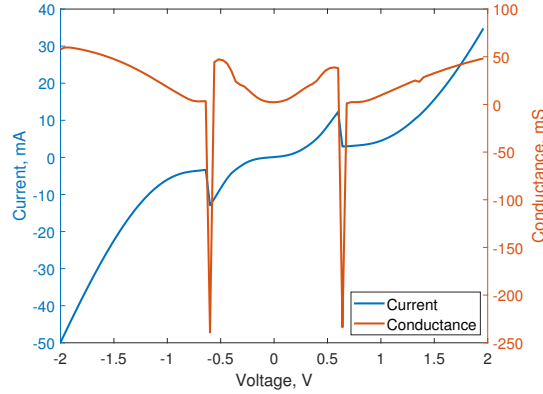


Figure 2.2: Experimental $I(V)$ characteristics of a double barrier heterostructure $Al_{0.33}Ga_{0.67}As/GaAs/Al_{0.33}Ga_{0.67}As$ at 77K. The emitter and the collector are constituted by Si-doped $GaAs$ ($1.1 \times 10^{17} cm^{-3}$). [From my experimental project in Paris Diderot, September 2019.]

In this respect, it is worth to stress that resonant tunnelling is a dynamic process and that in order for the Fabry-Perot effect to occur it is necessary that the wavefunction builds up inside the well, that is the well must be filled up by electrons. It can be defined a transient time with time constant τ_0 for the system to approach this condition [12]. Reasonably, this is related to the transmission through the barrier by:

$$\tau_0 = \frac{\hbar}{\Gamma_r} \quad (2.1)$$

where Γ_r is the Full Width at Half Maximum (FWHM) of the transmission through a barrier. This time constant should be compared with the one related to scattering τ . The principal effects of collisions are to decrease the peak transmission by the ratio $\frac{\tau_0}{\tau_0 + \tau}$ and to broaden the resonance because of the introduction of non-coherences. To summarize, in order to have coherent resonant tunnelling:

$$\Gamma_r \geq \Gamma_c \quad (2.2)$$

where $\Gamma_c = \frac{\hbar}{\tau}$ is the collision broadening [9].

2.2 Superlattices: does (mini)band transport always occur?

A periodic repetition of two layers of different materials (the two materials have to act as well and barrier according to band alignment) coupled by tunnelling makes each resonant transmission peak split in N transmission peaks (fig.2.3) where N is the number of coupled wells. This particular heterostructure is called (finite) **superlattice** and it has been studied by Tsu and Esaki[10]. For an ideally infinite superlattice, the splitting becomes infinitesimal leading in fact to *minibands*. In this case, a 1-D crystal is formed and Bloch theorem holds.

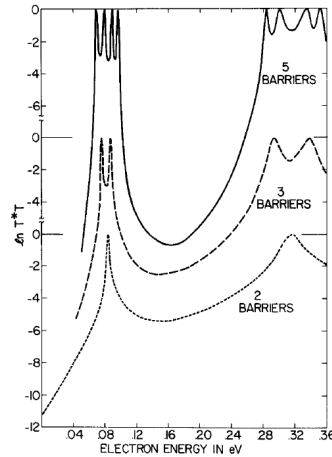


Figure 2.3: Transmission in logarithmic scale as a function of the electron energy for a superlattice with 1,3 and 5 periods (one period is constituted by one well and one barrier). The barrier and well thicknesses are 20 Å and 50 Å, respectively. The barrier height is 0.5 eV. From [10].

The structure is called superlattice because it is a second level of periodicity superimposed on the first level, which is the crystalline nature of the semiconductors. The period is longer and the periodic potential weaker with respect to the constituting crystals. This is why the bandwidth of the arising minibands is in a much lower scale of energies and the Brillouin zone (BZ) narrower with respect to the band structures of the constituent materials. A simple model to describe a 1-D infinite superlattice is the Kronig-Penney model (fig.2.4a).

In this model, within the effective mass approximation, the system is described by the following equation[13]:

$$\cos(k_z d) = \cos(\alpha t_W) \cosh(\beta t_B) + \frac{1}{2} \left(\frac{m_W^* \beta}{m_B^* \alpha} - \frac{m_B^* \alpha}{m_W^* \beta} \right) \sin(\alpha t_W) \sinh(\beta t_B) \quad (2.3)$$

where $\alpha^2 = \frac{2m_W^* E}{\hbar^2}$ and $\beta^2 = \frac{2m_B^* (V_0 - E)}{\hbar^2}$. $d = t_W + t_B$ is the superlattice period, k_z is the wavevector along the growth direction, E is the energy taken from the conduction band edge of the well material, t_W and t_B are the thicknesses of the well and barrier material, m_W^* and m_B^* the two respective effective masses. Bands arise requiring that eq.2.3 is valid between -1 and +1 (fig.2.4). It can be seen from the inset of fig.2.4b that the bandwidth grows exponentially by reducing the thickness of the barrier.

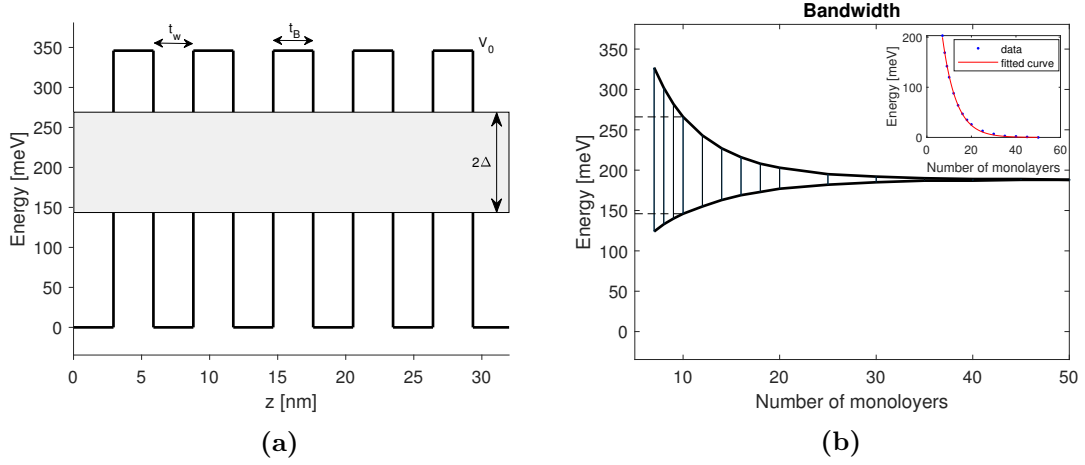


Figure 2.4: (a) Kronig-Penney simulated bandwidth of (10,10) $In_{0.53}Ga_{0.47}As/GaAs_{0.51}Sb_{0.49}$ superlattice's conduction band according to eq.2.3. The single confined level within each well couples with the one of the other wells forming a miniband. The notation (m,n) indicates that InGaAs is m monolayers (MLs) thick and GaAsSb is n MLs thick. Adopted parameters [from the group's database]: $m_W^* = 0.046 m_0$, $m_B^* = 0.054 m_0$, $t_W = t_B = 10$ MLs, $V_0 = 346$ meV (b) Variation of the top and bottom edges of the conduction miniband as a function of the MLs constituting the barrier. The well thickness is kept fixed at $t_W = 10$ MLs. The (10,10) band edges are prolonged with dotted lines to show the link with (a). Inset: bandwidth with exponential fitting.

For sufficiently weak coupling between wells (*tight-binding model*) the superlattice dispersion relation can be approximated by a sinusoidal form[14]:

$$E(k_z) = \Delta[1 - \cos(k_z d)] \quad (2.4)$$

For small electric fields the mobility can be shown to be [9]:

$$\mu_z = \frac{e \Delta d^2}{\hbar^2} \tau \quad (2.5)$$

in which $m^* = \frac{\hbar^2}{\Delta d^2}$ is the band-edge effective mass. Since the bandwidth Δ is dictated by transmission through the barrier, the effective mass rises with an increase of the barrier, layer thickness and effective masses of the two layers. The mobility for heavy holes and electrons may be therefore very different leading to a *mass-filtering* effect[9] where heavy-holes, generally characterized by a higher effective mass, actually remain localized. Transport proceeds by miniband conduction if the mean free path of the carriers appreciably exceeds the superlattice period and this requires that[9]:

$$\frac{\hbar}{\tau} < \Delta \quad (2.6)$$

Assuming $\tau \sim 1$ ps for holes [15], the bandwidth Δ should be greater than 0.7 meV. If eq.2.6 is not satisfied, superlattice's transport cannot be described by Bloch states. In the latter case, tunneling is rather a *phonon-assisted* process through localized states of adjacent wells (hopping transport). Considering phonon-assisted hopping as the leading transport mechanism, it can be shown that the mobility is given by[16]:

$$\mu = \frac{ed^2}{k_B T} \langle W \rangle \quad (2.7)$$

where $\langle W \rangle$ is the thermodynamically averaged phonon-assisted tunnelling rate.

Another possible transport mechanism different from tunneling is given by *thermionic emission*. It consists on diffusion of carriers through the continuum of states with energy higher than the barrier. The thermionic emission lifetime following [17] is given by:

$$\tau_{E,z} = \left(\frac{2\pi m_z^* t_w^2}{k_B T} \right)^{1/2} \exp \left[\frac{V_b}{k_B T} \right] \quad (2.8)$$

where t_w is the thickness of the well, m_z^* the effective mass along z. The conductivity through this mechanism is highly dependent on the temperature, on the barrier V_b seen by the quasi-bound carrier and on the diffusivity since a higher diffusivity may contrast the carrier trapping in an adjacent well. It is worth to underline that thermal assisted transport has to be regarded as a sequential process at the contrary of miniband which is extended throughout the superlattice.

2.3 Type-II superlattices and device's structure

Type-II superlattices (T2SL) are superlattices with type-II heterojunctions between the constituent materials suited to detect IR. T2SL detectors are minority carrier devices whose advantages and drawbacks have been already mentioned in the introduction (ch.1). The T2SL energy gap, which determines the cutoff wavelength of the detector, is given by the difference between the bottom of the lowest conduction miniband and the top of the highest hole miniband. The optical transition occurs close to the heterojunction between two layers, where the electron and hole wavefunctions, which are spatially separated in different layers, overlap.

Fig.2.5 shows schematically the pixel's structure of the detector investigated in this work with a detailed description below. The choice of InGaAs/GaAsSb T2SL allows to keep the

existing structure of the InGaAs on InP simply by substituting the n-doped bulk InGaAs with the n-doped T2SL. In this configuration, the known diffusion process of Zinc (p-dopant) allows to create a pn junction with the n-doped T2SL where the photogenerated holes are extracted. Therefore, the great interest of this work is about holes' transport properties that are in turn related to the valence band of the T2SL.

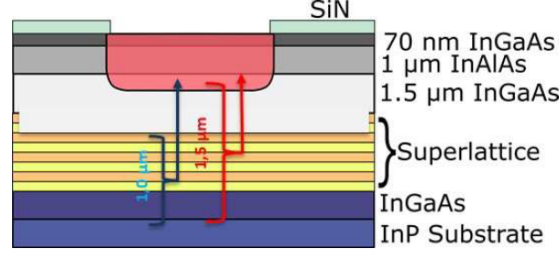


Figure 2.5: InGaAs/GaAsSb T2SL photodiode structure. The blue and red lines represent the absorption depth of a "blue" and a "red" wavelength since light impinges from the bottom. The red zone indicates the diffused Zn. The substrate is n-doped InP. The T2SL absorbing material is $1 \mu\text{m}$ thick. Between them, a 200 nm -thick n-InGaAs buffer layer acts as a screener of substrate defects. The thick ($1.5 \mu\text{m}$) n-InGaAs layer contains the photodiode depletion region and limits the GR dark current. The thick InAlAs cap (unintentionally n-doped $2 \times 10^{16} \text{ cm}^{-3}$) serves to minimise the diffusion current and to remove surface influences. The wafer is capped with a 70 nm InGaAs layer, which serves to (i) encapsulate and protect the InAlAs, which is prone to oxidation, (ii) aid Zn diffusion, due to the high solubility of Zn in InGaAs, and (iii) minimise the contact resistance to the p-type region.

A graphical summary of the working principle for a (5,5)InGaAs/GaAsSb T2SL is depicted in fig.2.6¹. The electron-hole pair creation induced by IR absorption is shown both in direct space and reciprocal space. Note that, while the absorption is indirect in real space, it is direct in k-space.

One of the main characteristics of T2SL and of superlattices, in general, is the *anisotropy* of the heavy hole and the light hole minibands that give the asymmetry of the bands between the [001] growth direction and the [100] in-plane direction (fig.2.6b). Let's consider the superlattice growth direction as z . Heavy holes, that can be seen as a combination of p_x and p_y orbitals, show lower effective mass along [100] with respect to light holes. The latter has mainly contribution from p_z and therefore show opposite behaviour with respect to heavy holes (see table A.2 for the description of zone-center states). Because of the heavier mass of heavy holes along the z -direction, the HH-LH degeneracy is removed (fig.2.7). The different curvature of the two bands along (k_x, k_y) would lead to a cross. However, considering a coupling, *anti-crossing* occurs. This brings to the so-called *HH-LH mixing effect* which may lead to much higher hole mobility along the growth direction[18]. This anisotropy is very important when considering imagers constituted by an array of pixels. Large anisotropies in hole mobility may lead to an increased *cross-talk* therefore ruining the imager resolution[19].

¹All the kind of graphs like in fig.2.6 have been made through a MATLAB code developed by me to analyse simulation outputs of **k·p** model (Appendix A) as described in section 3.2 of the next chapter.

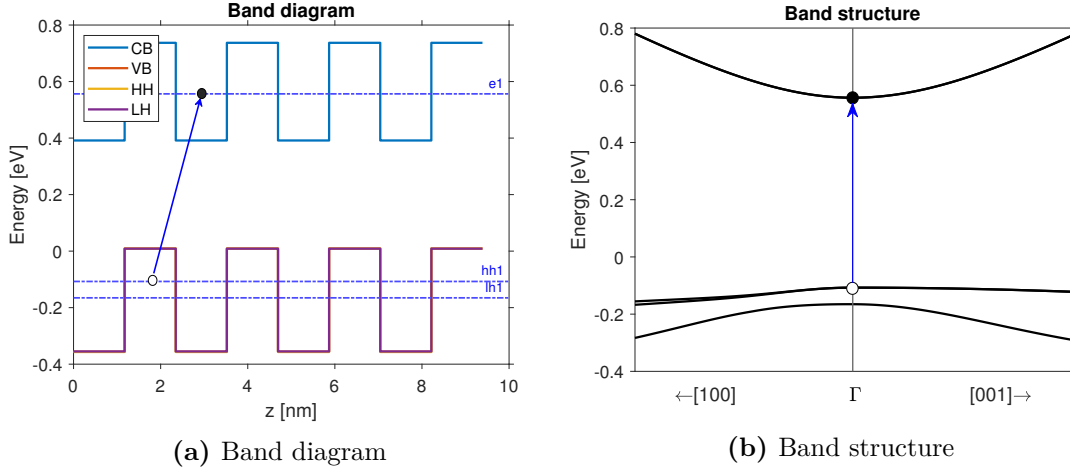


Figure 2.6: $\mathbf{k} \cdot \mathbf{p}$ simulated (a) Band diagram and (b) band structure of InP lattice-matched (5,5)InGaAs/GaAsSb T2SL. The band diagram shows how the band edge energy for Conduction Band (CB), Valence Band (VB), Heavy Hole (HH), Light Hole (LH) varies as a function of z . The band structure shows the energy bands as a function of \mathbf{k} for the directions k_z and k_x . The arrow represents the absorption of IR causing the generation of carrier. Just the bands close to the electronic gap are shown. In the band diagram, $e1$, $hh1$ and $lh1$ represent the value of the first conduction band, the first topmost and the second topmost valence bands respectively in Γ . The gap of the superlattice is given in this case by $e1-hh1$. The computed effective masses of heavy holes along $[100]$ and $[001]$ are $-0.05 m_0$ and $-0.83 m_0$ respectively.

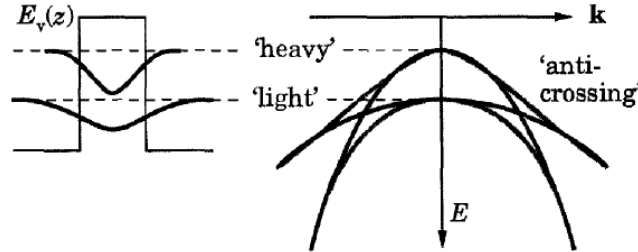


Figure 2.7: Removal of valence band degeneracy and mixing effect in quantum wells. From [20].

The Kronig Penney model, adopted here as a baseline to illustrate electronic properties of superlattices, does not consider effects like anti-crossing and non-parabolicity of bands and this is the reason why more accurate models like $\mathbf{k} \cdot \mathbf{p}$ are adopted.

Chapter 3

Results

3.1 Experimental quantum efficiency spectra

Experimental results, obtained by the group prior to my arrival at III-V lab, regard measures of Quantum Efficiency (QE) on the devices whose absorbing materials are listed in table 3.1. Actually, the period of the superlattices should have been symmetric (3nm/3nm, 5nm/5nm, 7nm/7nm) but, due to a mistake in the growth program, the InGaAs thickness remained unchanged. These three devices showed simulated cutoff wavelengths of $2.1 \mu m$, $2.3 \mu m$ and $2.5 \mu m$ respectively. Fig.3.1 illustrates a comparison between the spectral QE of bulk InGaAs on InP detector (ART3993) and two T2SL photodiodes (ART4013 and ART4015) at different temperatures. It is recalled that the QE for a pn-junction photodiode is given by[21]:

$$\eta = (1 - R) \left[1 - \frac{e^{-\alpha W_D}}{1 + \alpha L_p} \right] \quad (3.1)$$

where R is the reflection coefficient, α the absorption, W_D the depleted region width and L_p the diffusion length of the minority carriers.

The work I conducted concerned the analysis of such spectra with the aim of finding the underlying physical problems (exposed in ch.2) and suggest solutions aided by **k**·**p** simulations.

As it can be noted, there are two main differences between the bulk and the T2SL QE spectra: one is the shape and the other is the temperature dependence. The cutoff wavelength λ_c of bulk InGaAs is about $1.65 \mu m$. Looking at T2SL spectra (ART4013 and ART4015) at given wavelength greater than $1.65 \mu m$, which is the region where the T2SL is designed to absorb, the QE is characterized by an exponential dependence on temperature of the kind $\sim \exp\left(-\frac{E_a}{k_B T}\right)$ where E_a is the *activation energy*. This suggests that transport is thermally-activated rather than described by band structure implying that holes are actually localized. This hypothesis is confirmed also by the slanting curve for $\lambda \leq 1.6 \mu m$. Such energetic photons are absorbed by bulk InGaAs and GaAsSb nearby the substrate where generated carriers are hindered from reaching the p-contact.

Wafer	Description
ART3993	<i>InGaAs bulk absorber of 3 μm</i>
ART4013	<i>T2SL 165 repeats of 3nm/3nm InGaAs/GaAsSb</i>
ART4014	<i>T2SL 100 repeats of 3nm/5nm InGaAs/GaAsSb</i>
ART4015	<i>T2SL 70 repeats of 3nm/7nm InGaAs/GaAsSb</i>

Table 3.1: Tested SWIRUP T2SL at III-V lab. All the T2SLs are in lattice-matched condition with the InP substrate: this corresponds to an *In* concentration in InGaAs of 53% and an *As* concentration in GaAsSb of 51%.

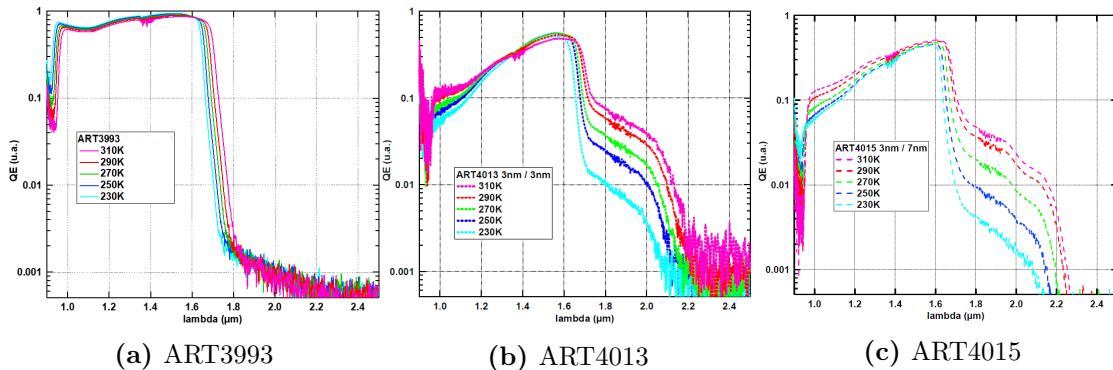


Figure 3.1: Quantum Efficiency for ART3993, ART4013 and ART4015 devices in logarithmic scale with temperature as parameter.

3.2 Localization analysis through kp simulations

In order to study new structures of T2SL as absorbing material, I interpreted my simulation results according to the discussion I made in section 2. The holes generated by IR absorption in the T2SL, which is located outside the depleted region of the pn junction (fig.2.5), reach the p-contact through diffusion since no voltage is applied to the active region. Therefore, to increase the quantum efficiency (eq.3.1) an high diffusion length is needed. The diffusion length along the growth direction is given by $L_{p,z} = \sqrt{D_z \tau_r}$ with the diffusivity $D_{p,z} = \frac{k_B T}{e} \mu_{p,z}$ and the mobility μ given by eq.2.5 in case of band transport; τ_r is the hole lifetime.

Since the mobility depends on the bandwidth of the miniband, I oriented my simulations towards the increase of the bandwidth (and therefore the reduction of the effective mass) for cutoff wavelengths as close as possible to 2.5 μm . In order to simulate $\text{In}_x\text{Ga}_{1-x}\text{As}/\text{GaAs}_y\text{Sb}_{1-y}$ T2SL I used a 18×18 $\mathbf{k}\cdot\mathbf{p}$ model described in section A.2 exploiting a code made in III-V lab. I wrote a simple MATLAB code to extrapolate further informations from the simulation results and to make plots. The simulation output two text files: one containing the band structure and the other containing the band diagram. Besides these two outputs, the simulation displayed as results the strain of the layers, the band-edge effective masses along specific directions and the energy gap in Γ . All the other quantities mentioned in the following, like energy gaps and band offsets come from my MATLAB code. All the simulations are performed at 300K. I want to remark that a complete design

of a new structure would have required absorption simulations and also the consideration of scattering mechanisms. However, codes for these tasks were not available¹ and actually band structure-derived properties were enough for the purpose of this work.

The first thing I did was to simulate the device ART4013 to try to understand the reason of localization. The band diagram and the band structure are shown in fig.3.2. Focusing on fig.3.2b, the topmost valence band, which corresponds to the Heavy Hole (HH) one, is almost flat resulting in a large effective mass ($-9.9m_0$) and negligible Band Width (BW) along the growth direction k_z . The cutoff wavelength, that is computed from the superlattice bandgap $E_g = e1 - hh1$, is given by $\lambda_c [\mu m] = \frac{1.24}{E_g [eV]}$ and in the case of T2SL ART4013 corresponds to $2.1 \mu m$. All these quantities are reported in tab.3.2 for the three T2SL photodiodes of table3.1.

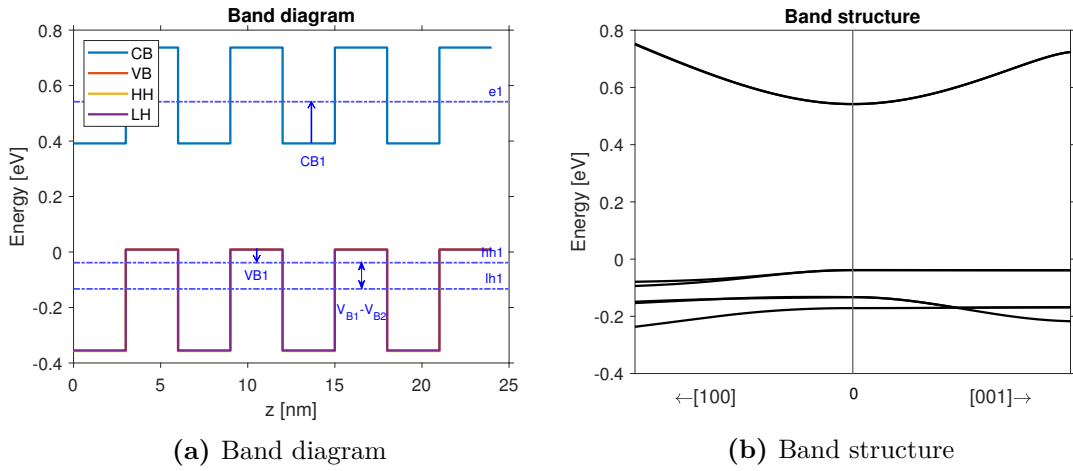


Figure 3.2: $\mathbf{k}\cdot\mathbf{p}$ simulated (a) Band diagram and (b) band structure for device ART4013.

The most important parameters here to understand localization are effective mass and bandwidth of the first heavy hole miniband of the superlattice. According to the discussion of the previous section, this may be a clear suggestion that this device probably suffered from hole localization.

Device	$\lambda_c [\mu m]$	$m_{v1,z} [m_0]$	V_{B1}	C_{B1}	BW	$V_{B1} - V_{B2}$
ART4013	2.1	-10	48	150	0.5	95
ART4014	2.1	-34	22	182	0.0	64
ART4015	2.1	-19	13	199	0.1	37

Table 3.2: Some $\mathbf{k}\cdot\mathbf{p}$ -simulated band properties of T2SL photodiodes of table 3.1. λ_c is the cutoff wavelength, $m_{v1,z}$ is band-edge effective mass of the topmost valence miniband along direction k_z , BW is the bandwidth of the topmost valence miniband along k_z (note that it is $\sim 0 meV$). For the other quantities, refer to fig.3.2. Energies are expressed in meV; m_0 is the electron rest mass.

To improve transport properties, first I investigated the effects of InGaAs and GaAsSb

¹Coding of these phenomena will constitute my next task during my training at III-V Lab.

layers' thicknesses on the band features for a InP-lattice matched T2SL. Fig.3.3a displays the variation of the cutoff wavelength with the period's thickness which is varied as described in the caption of the figure. It is immediately clear that the increase of the GaAsSb thickness does not bring to any advantage since it causes a blueshift of the gap and an increase of the effective mass with consequent reduction of the bandwidth. This is why also the other T2SLs of table 3.1 experimentally show localization in the QE. In particular, ART4013 shows an activation energy at $1.8 \mu\text{m}$ of 150 meV while ART4015, with 7nm of GaAsSb, shows an activation energy of 200 meV at the same wavelength. On the contrary, increasing the InGaAs thickness or both the thicknesses of the two layers at the same time brings to a redshift of the gap and an increase of the effective mass leading to a tradeoff. Fig.3.3b shows the effective mass as a function of the cutoff wavelength for several configurations where the two layers' thicknesses are varied at the same time.

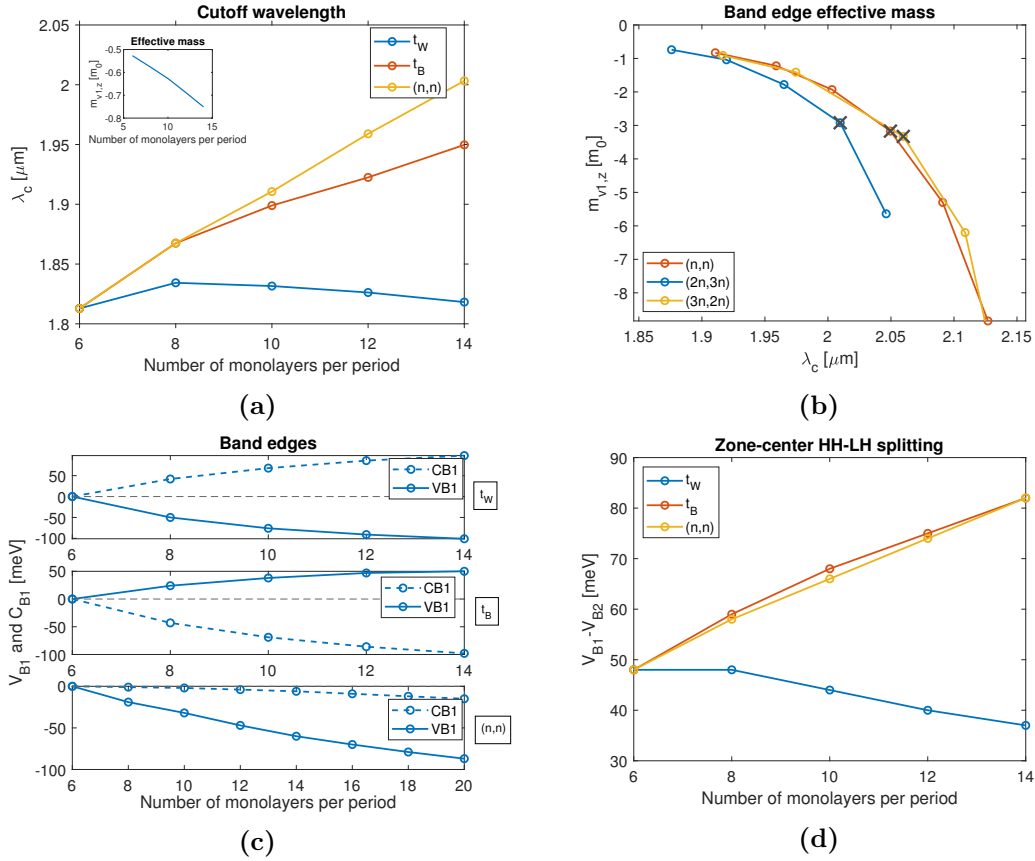


Figure 3.3: Simulated quantities for $\text{In}_{0.53}\text{Ga}_{0.47}\text{As}/\text{GaAs}_{0.51}\text{Sb}_{0.49}$ T2SL (a) Cutoff wavelength (inset: $m_{v1,z}$ for the t_W curve case), (b) topmost valence miniband band edge effective mass. Crosses indicate points where $BW \sim 2 \text{ meV}$ (c) C_{B1} and V_{B1} with respect to their initial values (d) $V_{B1} - V_{B2}$. t_W stands for well thickness while t_B for barrier thickness. The terms 'well' and 'barrier' refer to holes: the well is the GaAsSb layer while the InGaAs constitutes the barrier. The t_W curve means that t_W is varied keeping fixed t_B to 3 MLs; same approach for the t_B curve. In the (a^*n, b^*n) case, both the layer thicknesses are varied at the same time. The thickness of one monolayer is about 2.93 \AA for both InGaAs and GaAsSb.

Since the difference between the conduction band edge of InGaAs and the valence band edge of the GaAsSb is fixed (eq.3.3), the variation of the gap is given by the variation of C_{B1} and V_{B1} (please refer to fig.3.2a for the notation). The latter are represented in fig.3.3c for the three cases of fig.3.3a. In $t_B = 3MLs = const$, the blueshift is caused by a faster increase of C_{B1} with respect to the decrease of V_{B1} . In the case of $t_W = 3MLs = const$ the behaviour of V_{B1} and C_{B1} is reversed: C_{B1} decreases faster than the increase of V_{B1} . In the (n,n) case, C_{B1} remains almost constant while V_{B1} decreases causing the redshift. The steeper variation of C_{B1} with respect of V_{B1} is given by the lower effective mass of the electron with respect to the heavy hole one. However, the maximum reachable cutoff wavelength with such approach is about $2.05\mu m$ as indicated by the crosses in fig.3.3b for the (n,n) and (3n,2n) configurations and therefore a complementary strategy is needed to further increase the λ_c 's upper limit.

3.2.1 Introduction of strain

Considering $In_xGa_{1-x}As/GaAs_ySb_{1-y}$ on InP substrate, according to the values of x and y , the constituting layers may be strained (fig.3.4). When $x = 53\%$ and $y = 51\%$, the structure is lattice-matched. The lattice constant of the structure is determined by the substrate that in this case is InP (5.87 \AA). In order to build strained structures without introducing defects (pseudomorphic growing), *strain-compensation* growth technique is used. It consists of alternating layers with the opposite type of strain. This means that if one layer is tensile stressed, the other must be compressed or vice versa and the two strains must compensate each other.

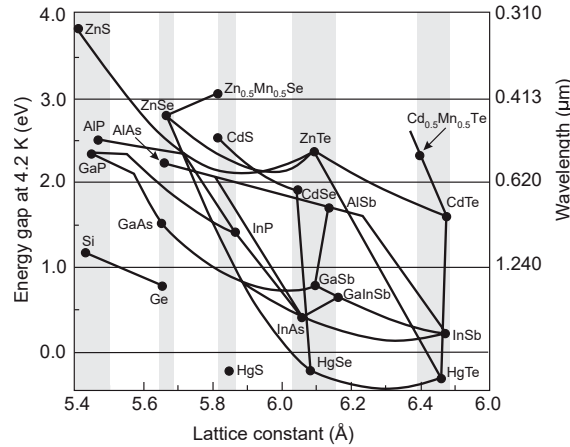


Figure 3.4: Energy gap at 4.2K as a function of lattice constant for binary alloys (full points). The line interpolating two points show how the dependence holds for ternary alloys. GaAsSb lies between GaSb and GaAs while InGaAs between InAs and GaAs. For $x=0.53$ and $y=0.51$ the two ternaries are naturally lattice-matched to InP. On the right side of the InP lattice constant, the ternary is compressed while on the left side is stretched. From [22].

The way strain affects band edges in Γ in direct-bandgap semiconductors is depicted in fig.3.5. As it can be seen, strain leads to HH-LH splitting in the bulk band structure. Moreover, the gap changes: with compression bonds are shorter than as they would be

without lattice-matched condition leading to an increase of the energy gap; the opposite occurs with tensile strain. Since both InGaAs and GaAsSb remain direct-gap materials over their entire composition range, these properties can be properly exploited to tailor the electronic characteristics of T2SLs. In particular, I investigated both the GaAsSb in compression (InGaAs in extension) and the GaAsSb in extension (InGaAs in compression).

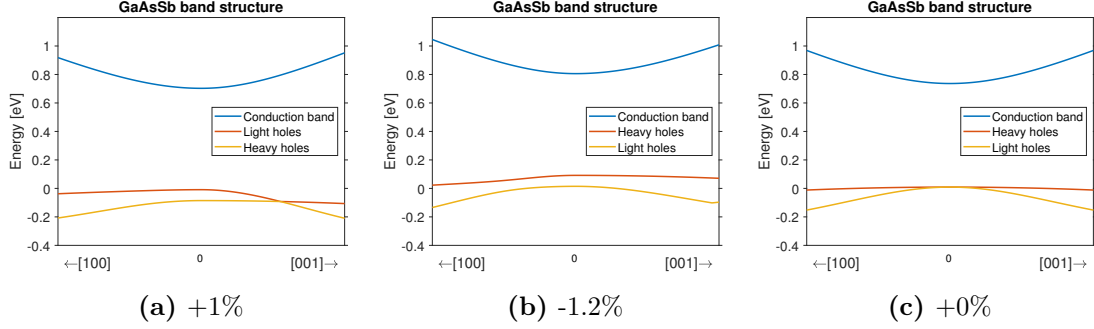


Figure 3.5: $\mathbf{k}\cdot\mathbf{p}$ simulated GaAsSb band structure under different values of biaxial strain. The caption of each graph indicates the amount of strain in percentage (parts per hundred). The HH-LH splitting is positive with biaxial compression and negative with biaxial tension.

The degrees of freedom I had to design the proper T2SL were the thicknesses of the two layers and the composition. Moreover, strain-compensation requires:

$$\frac{1}{t_W + t_B} |t_W \times strain_W + t_B \times strain_B| = 0 \quad (3.2)$$

which in fact reduces the degree of freedom. In the formula, $strain_{W(B)}$ represents the strain of the W(B) layer. Remember that in this case, I call 'well'(W) the GaAsSb layer while 'barrier'(B) the InGaAs layer since I refer to holes.

In this respect, once analysed the role of t_W and t_B in the electronic properties of T2SL, I investigated the role of layers' composition.

The band-edge alignment is derived experimentally from the valence band edge discontinuity $V_P(z)$ and the band gaps of the unstrained constituent materials and then adding the effect of the strain. Setting $V_P = 0$ for a reference material (GaAs in my case), the conduction band edge variation according to the growth direction z is given by:

$$V_S(z) = V_P(z) + E_g(z) - E_g(GaAs) \quad (3.3)$$

The band edges enter in the $\mathbf{k}\cdot\mathbf{p}$ model as inputs (Appendix A). For a review on III-V semiconductor band parameters refer to [23].

GaAsSb in compression

Since the rise of λ_c towards $2.5 \mu m$ by increasing the number of monolayers per period is not practicable because of the fastly growing hole effective mass (fig.3.3b), I first tried to investigate how band edges of GaAsSb vary sweeping $y = 0.51 \rightarrow 0$ (GaAsSb in compression) since holes reside in GaAsSb. In this respect, keeping $x=0.53$ fixed to make the comparison more clear, I noticed an increase of the gap of strained GaAsSb of about 126 meV from

$y=0.50$ to $y=0.05$ which goes in an increase of 280 meV of the Conduction Band edge Offset (CBO) and an increase of 154 meV of the Heavy Hole band edge Offset (HHO) as it can be seen in the band-edge alignment of fig.3.6a. The increase of the valence band edge in GaAsSb towards the conduction band edge of InGaAs makes this a potential solution for the reduction of the gap keeping the thickness of the layers fixed. Then I considered the variations in the InGaAs band edges when put in tensile strain. The effect of bands alignment, sweeping $x = 0.50 \rightarrow 0.05$ with $y = 0.51$, is an increase of the InGaAs gap who mostly goes in an increase of HHO while CBO remains almost constant (fig.3.6a)². Fig.3.7 shows these offsets on the band diagram. As the role of tensile-strained InGaAs is just to increase HHO and therefore the potential barrier seen by holes while keeping the CB edge fixed, this brought me to find the best y in order to lower as much as possible the gap and then to choose x according to eq.3.2. Refer to table3.3 for the specific strain of the two layers.

As depicted in fig.3.6b, by just analysing the effect of *As* concentration while keeping the *In* one fixed to 53%, C_{B1} increases while V_{B1} remains almost constant. This means that, in order for the gap to decrease, $\Delta(C_{B1}) - \Delta(HHO) + \Delta(V_{B1}) < 0$ must be verified. From fig.3.6c the gap redshifts from $y = 50\%$ up to $y = 15\%$ and blueshifts for $y < 15\%$ concluding that the maximum optimization may be reached at $y = 15\%$.

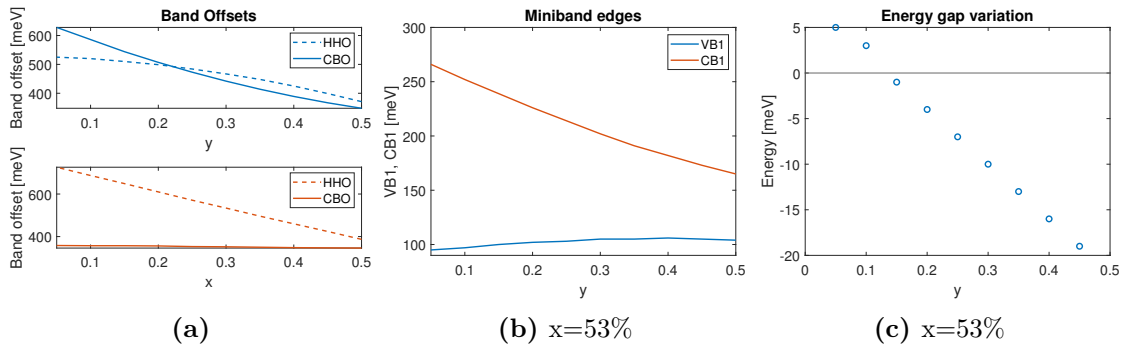


Figure 3.6: Some useful simulated band parameters for $(5,5)In_xGa_{1-x}As/GaAs_ySb_{1-y}$ T2SL. (a) HHO and CBO band offsets (b) Top most valence band edge and first-conduction band edge in Γ (c) Superlattice energy gap variation.

Therefore, I oriented myself towards this direction performing simulations of some promising SWIRup that I proposed to the crystal grower of the group and that are listed in tab.3.4. Again, the *In* concentration is subordinated to the *As* one to guarantee strain-compensation.

The general trend for both the cutoff wavelength λ_c and of the effective mass of the topmost valence miniband along the growth direction $m_{v1,z}$ as a function of the number of monolayers n is a monotonic grow. Therefore, it is useful to plot the behaviour of the effective mass as a function of the wavelength to understand which composition gives

²I remark that the real structure must satisfy the strain-compensation (eq.3.2); this "graphical" analysis is just to ascertain how band edges align in the band diagram in order to have some intuitions on the resulting band structure properties.

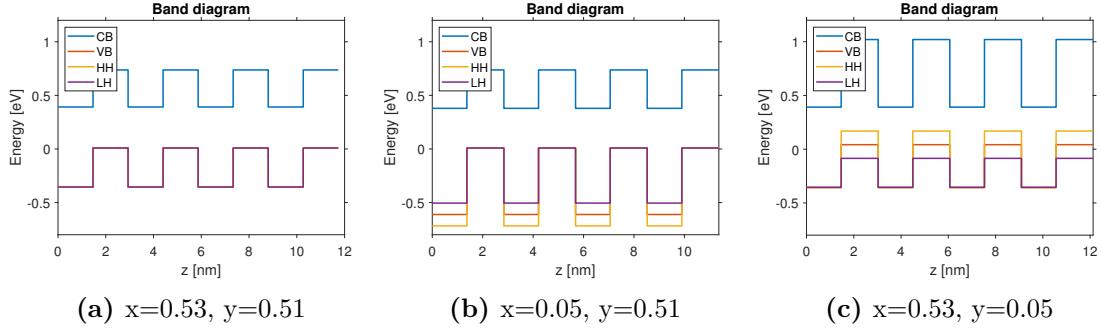


Figure 3.7: Effect of strain on the band edges of InGaAs and GaAsSb compared to the unstrained case. (a) lattice-matched (b) GaAsSb in maximum compression with InGaAs lattice-matched (c) InGaAs in maximum extension with GaAsSb lattice-matched. Note that the graphs are aligned in energy to favour the comparison with the lattice-matched case.

Band offsets [meV]: (a) VBO=365, CBO=346; (b) VBO=620, CBO=358 VB splitting=106; (c) VBO=398, CBO=628, VB splitting=127.

Layer	Concentration									
	0.5	0.45	0.4	0.35	0.3	0.25	0.2	0.15	0.10	0.05
$In_xGa_{1-x}As$	0.2	0.6	0.9	1.3	1.6	2.0	2.4	2.7	3.1	3.5
$GaAs_ySb_{1-y}$	-0.1	-0.5	-0.8	-1.2	-1.6	-1.9	-2.3	-2.7	-3.0	-3.4

Table 3.3: Biaxial strain in percentage for $In_xGa_{1-x}As$ ($GaAs_ySb_{1-y}$) as a function of x(y) concentration. When positive, it is tensile strain while for negative is compressive strain.

Device	x	y	n	λ_c [μm]	$m_{v1,z}$ [m_0]	$V_{B1} - V_{B2}$ [meV]
#1.1	0.1	0.05	4	2.13	-1.42	not shown
#1.2	0.1	0.05	5	2.13	-1.81	
#1.3	0.1	0.05	6	2.20	-3.26	
#1.4	0.1	0.05	7	2.28	-5.82	
#1.5	0.1	0.05	8	2.35	-9.68	
#2	0.15	0.10				not shown
#3.1	0.2	0.15	4	2.11	-1.15	165
#3.2	0.2	0.15	5	2.15	-1.66	176
#3.3	0.2	0.15	6	2.21	-2.95	188
#3.4	0.2	0.15	7	2.29	-5.3	197
#3.5	0.2	0.15	8	2.37	-9.08	189
#4	0.25	0.2				not shown
#5	0.3	0.25				not shown
#6.1	0.35	0.3	4	2.04	-0.9	119
#6.2	0.35	0.3	5	2.09	-1.34	130
#6.3	0.35	0.3	6	2.16	-2.28	141
#6.4	0.35	0.3	7	2.23	-4.04	150
#6.5	0.35	0.3	8	2.30	-7.12	156

Table 3.4: Simulated $(n, n)In_xGa_{1-x}As/GaAs_ySb_{1-y}$ strain-compensated T2SL. For each composition, 5 values of n are considered.

the lower effective mass at a given wavelength. The graph, obtained from simulated data of table 3.4 is depicted in fig.3.8a. Device #3 ($x=20\%$, $y=15\%$) shows the best characteristics. In fact, the associated curve tends to be above the other strain-compensated structures. Note also the big advantage with respect to the lattice-matched one. Of

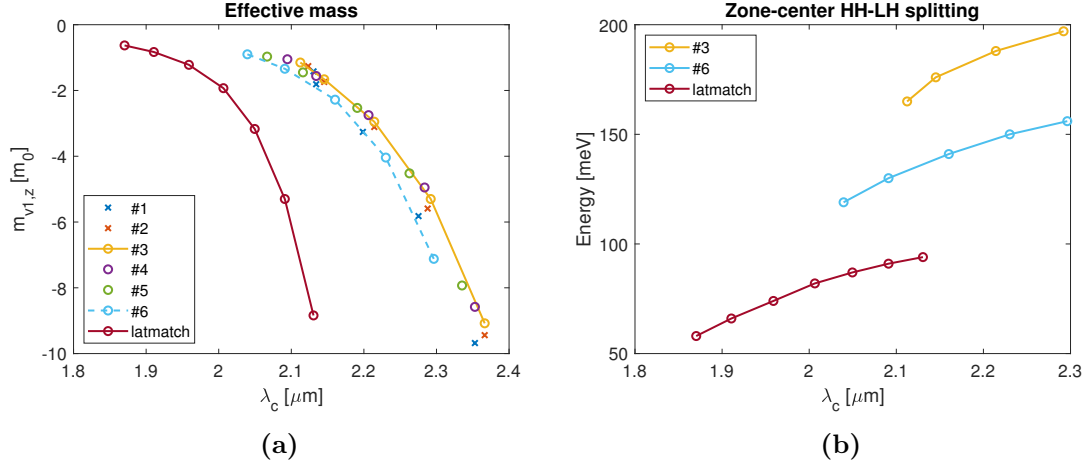


Figure 3.8: $\mathbf{k}\text{-p}$ simulated (a) Effective mass and (b) zone-center HH-LH splitting as a function of cutoff wavelength for devices of tab.3.4. Lattice-matched # is also shown for direct comparison.

course, since the offsets are bigger in the strained cases, the effective mass increases (in absolute value) with a higher rate as a function of n with respect to the unstrained case. Another advantage of using GaAsSb in compression, besides the lowering of the gap, is the higher topmost valence band edge splitting in Γ that is known to lead to an higher mobility because of reduced interband scattering mechanisms (fig.3.8b)[4]. In this solution, heavy holes experience an higher barrier $V_b = HHO - V_{B1}$ with respect to the lattice-matched case. This is expected to lower the thermal activated transport. For example, $V_b = 250 \text{ meV}$ for $(4,4)\text{In}_{0.53}\text{Ga}_{0.47}\text{As}/\text{GaAs}_{0.51}\text{Sb}_{0.49}$ and $V_b = 625 \text{ meV}$ for $(4,4)\text{In}_{0.20}\text{Ga}_{0.80}\text{As}/\text{GaAs}_{0.15}\text{Sb}_{0.85}$.

GaAsSb in extension

In order to have GaAsSb in extension in strain-compensated structures, it is needed that $x, y \rightarrow 1$.

Layer	Concentration								
	0.55	0.60	0.65	0.70	0.75	0.80	0.85	0.90	0.95
$\text{In}_x\text{Ga}_{1-x}\text{As}$	-0.1	-0.5	-0.8	-1.1	-1.5	-1.8	-2.1	-2.5	-2.8
$\text{GaAs}_y\text{Sb}_{1-y}$	0.3	0.7	1.1	1.4	1.8	2.2	2.6	3.0	3.4

Table 3.5: Biaxial strain in percentage for $\text{In}_x\text{Ga}_{1-x}\text{As}$ ($\text{GaAs}_y\text{Sb}_{1-y}$) as a function of x(y) concentration. When positive, it is tensile strain while for negative is compressive strain.

The table 3.5 shows the strain in percentage of the two layers as a function of the concentrations x,y. A hint of how energy levels and gaps of superlattice will evolve with GaAsSb in extension can be seen by the evolution of band offsets in fig.3.9. Changing $x, y \rightarrow 1$, the VBO is much lower with respect to the unstrained case and this may favour thermal-assisted transport. However, the increase of CBO due to $x \rightarrow 1$ is lower than the decrease of HHO(=VBO+VB splitting) due to $y \rightarrow 1$ (fig.3.9) and therefore a blueshift of

the superlattice gap occurs with respect to the unstrained case as expected (fig.3.10a). The intriguing thing with GaAsSb in extension is that the bulk zone-center HH-LH splitting becomes negative (fig.3.5a) and interesting properties may arise in the energy difference between hh1 and lh1. From $\mathbf{k}\cdot\mathbf{p}$ simulations, the hh1-lh1 splitting reaches the order of $k_B T$ as indicated in fig.3.10a and, following the argument of Ting[4], this may lead to two effects on the hole mobility. The first is the increased interband scattering probability which ruins the coherence of the miniband transport; the second is an enhanced HH-LH mixing effect which may enhance the hole mobility.

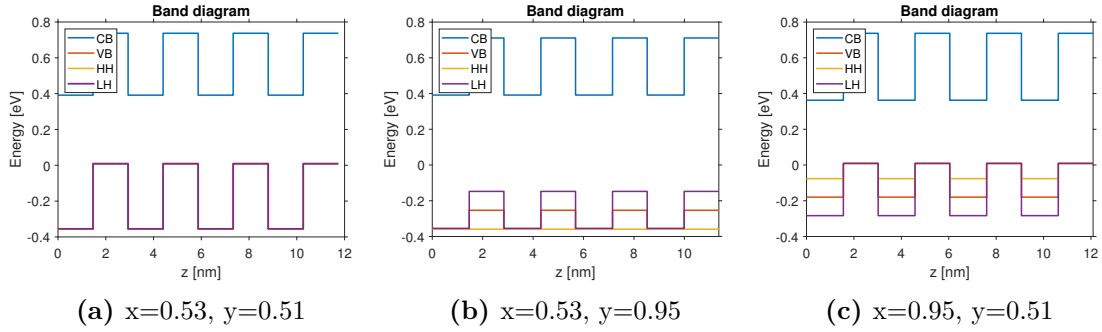


Figure 3.9: Effect of strain on the band edges of InGaAs and GaAsSb compared to the unstrained case. (a) lattice-matched (b) GaAsSb in maximum extension with InGaAs lattice-matched (c) InGaAs in maximum compression with GaAsSb lattice-matched. Note that the graphs are aligned in energy to favour the comparison with the lattice-matched.

Band offsets [meV]: (a) VBO=365, CBO=346; (b) VBO=103, CBO=319 VB splitting=106;(c) VBO=189, CBO=374, VB splitting=104.

Keeping x, y increasing towards 1, the HH zone-center state of compressive-strained InGaAs turns out to exceed in energy the one of GaAsSb causing, in fact, a type-II to type-I transition for heavy holes. This transition occurs for $0.75 \leq x \leq 0.80$ as indicated in fig.3.10a and it is shown for $x=y=85\%$ in fig.3.10b.

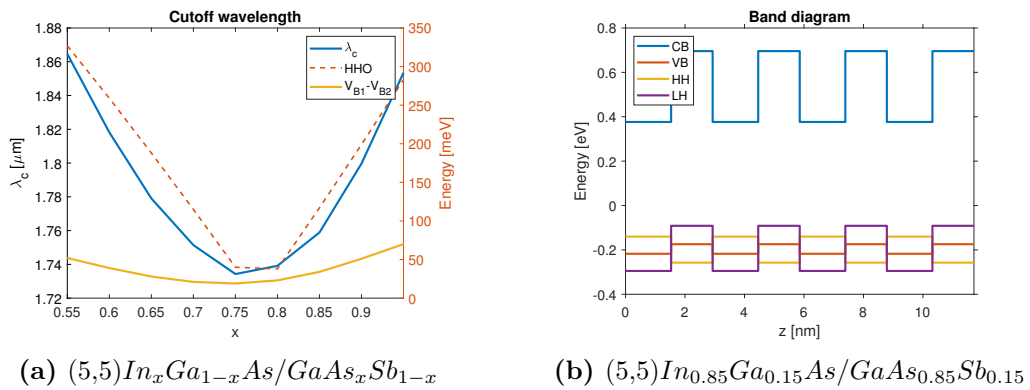


Figure 3.10: Type-II \rightarrow Type-I HH transition. $\mathbf{k}\cdot\mathbf{p}$ simulated (a) λ_c , HHO and $V_{B1} - V_{B2}$ (considering sign) as a function of x for $(5,5)In_xGa_{1-x}As/GaAs_xSb_{1-x}$ T2SL. (b) Band diagram for $x = y = 85\%$. The type-I is meant as formed by HH band edge profile (yellow line) and the conduction band edge profile.

Chapter 4

Conclusions

Quantum efficiency spectra of InGaAs/GaAsSb T2SL photodiode have been analyzed. In particular, the exponential dependence on temperature at a given wavelength in the T2SL suggested a problem of hole localization in the GaAsSb layer. In this respect, phonon-assisted tunneling and thermionic emission transport mechanisms have been suggested as leading transport mechanisms. To increase hole mobility, strain-compensated T2SL have been simulated through a 18×18 $\mathbf{k}\cdot\mathbf{p}$ model in order to make miniband transport the leading mechanism. Following this task, the bandwidth of the topmost valence band has been engineered to be as large as possible for cutoff wavelengths towards $2.5 \mu m$ following the minimum value of $1 meV$ as reference value. Accordingly, two types of strained structure have been considered. The configuration with GaAsSb in compressive strain is promising in reaching a sufficiently low topmost valence miniband edge effective mass along the growth direction for cutoff wavelengths greater than $2 \mu m$ with an increased topmost valence band splitting. For the GaAsSb tensile strained configuration, the consequences of the heavy hole-light hole splitting of the order of $k_B T$ need to be studied as from one side this disadvantages single miniband transport but on the other side, this may enhance the HH-LH mixing effect. In this respect, a 3D $E(\mathbf{k})$ would be useful. However, a blueshift of the superlattice gap occurs and therefore it turns out to be useless in the frame of the SWIRup project.

In this work, just stationary properties have been considered. Scattering mechanisms and absorption coefficient should also be considered for a complete description. Programs performing such tasks will be coded in the next days.

Moreover, the results should be considered as semiquantitative. In fact, the $\mathbf{k}\cdot\mathbf{p}$ model is a perturbative approach that relies on a database of input parameters that is continuously updated to the new literature and experiments.

Following the results of this work, new devices will be produced and tested in the next growth campaign.

Appendices

Appendix A

kp model

The $\mathbf{k}\cdot\mathbf{p}$ model is a method that allows to compute band structures of bulk and heterostructure materials by making use of few parameters like optical matrix elements and energy gaps that can be obtained directly or indirectly from experiments. Matrix elements, in particular, are determined by fitting the experimental effective masses with the model, i.e. finding those values that give the simulated effective masses as close as possible to the experimental ones.

The model considers within a certain level of approximation features like nonparabolicity, anisotropy and coupling between HH and LH bands[20].

This appendix is organized as follows: first a quick overview of the $\mathbf{k}\cdot\mathbf{p}$ in zinc-blende crystals with some reference to group theory is presented; secondly, the actual model employed in the simulations is discussed. A good approach towards $\mathbf{k}\cdot\mathbf{p}$ model and group theory can be found in [24].

A.1 Bulk

In the case of a bulk crystal with periodic potential the eigenstates are given by the Bloch theorem:

$$\Psi_{n\mathbf{k}}(\mathbf{r}) = e^{i\mathbf{k}\cdot\mathbf{r}} u_{n\mathbf{k}}(\mathbf{r}) \quad (\text{A.1})$$

where n is the band index and \mathbf{k} the wavevector. The Bloch function $u_{n\mathbf{k}}(\mathbf{r})$ has the same periodicity as the unit cell. Substituting in the single-electron stationary Schroedinger equation:

$$\left[\frac{\hat{\mathbf{p}}^2}{2m_0} + V(\mathbf{r}) \right] \Psi_{n\mathbf{k}}(\mathbf{r}) = E_{n\mathbf{k}} \Psi_{n\mathbf{k}}(\mathbf{r}) \quad (\text{A.2})$$

a Schroedinger-like equation in $u_{n\mathbf{k}}(\mathbf{r})$ is obtained:

$$\left[\frac{\hat{\mathbf{p}}^2}{2m_0} + V(\mathbf{r}) + \frac{\hbar}{m_0} \mathbf{k} \cdot \mathbf{p} + \frac{\hbar^2 k^2}{2m_0} \right] u_{n\mathbf{k}}(\mathbf{r}) = E_{n\mathbf{k}} u_{n\mathbf{k}}(\mathbf{r}) \quad (\text{A.3})$$

Note that $H = H_0 + W(\mathbf{k})$ and therefore the term $W(\mathbf{k})$ can be treated as perturbation with respect to the known problem in Γ ($\mathbf{k}=\mathbf{0}$). Since the perturbation terms are proportional to k , the method works best for small values of k .

Nondegenerate band (one band model) For non degenerate states like the conduction band in Γ for zinc-blende semiconductors, nondegenerate perturbation theory can be applied to compute the dispersion relation analytically. To second order, $E_{n\mathbf{k}} = E_{n\mathbf{0}} + \frac{\hbar^2 k^2}{2m^*}$, where

$$\frac{1}{m^*} = \frac{1}{m} + \frac{2}{m^2 k^2} \sum_{n' \neq n} \frac{|\langle u_{n\mathbf{0}} | \mathbf{k} \cdot \mathbf{p} | u_{n'\mathbf{0}} \rangle|^2}{E_{n\mathbf{0}} - E_{n'\mathbf{0}}} \quad (\text{A.4})$$

is the *effective mass*. The matrix elements $\langle u_{n\mathbf{0}} | \mathbf{k} \cdot \mathbf{p} | u_{n'\mathbf{0}} \rangle$ different from zero are given by the matrix-element theorem which is based in the symmetry of the basis Bloch functions $u_{n\mathbf{k}}$ [24]. For example, the conduction band s-like states transform according to the irreducible representation Γ_1 of the point group T_d while the p-like valence band states according to Γ_4 . Note that the importance of other bands with respect to the considered n-th one depends on the energy difference therefore distant bands have lower contribution.

Degenerate bands and multiband model For the degenerate states like the valence band at Γ of zinc-blende, degenerate perturbation theory has to be used. As previously mentioned, the symmetry of the wavefunctions for such states is p-like and the states are usually denoted $|X\rangle$, $|Y\rangle$, $|Z\rangle$. In analogy with atomic physics, p orbital has an angular momentum associated to the quantum number $l=1$ and it's three-fold degenerate ($m_l = -1, 0, 1$). When spin is considered, an additional term H_{so} describing spin-orbit interaction is added. In this case, the symmetry of H_{so} and therefore of spin has to be considered. In tab.A.1 it is shown how the point group of zinc-blend T_d changes considering spin variable. The new group that contains also symmetry operations of spin wave functions is known as double groups. It is constituted by 48 elements divided in eight classes.

Irreducible representation	{E}	{ $3C_2/3\hat{E}C_2$ }	{ $6S_4$ }	{ $6\sigma/6\hat{E}\sigma$ }	{ $8C_3$ }	{ \hat{E} }	{ $6\hat{E}S_4$ }	{ $8\hat{E}C_3$ }
Γ_1	1	1	1	1	1	1	1	1
Γ_2	1	1	-1	-1	1	1	-1	1
Γ_3	2	2	0	0	-1	2	0	-1
Γ_4	3	-1	-1	1	0	3	-1	0
Γ_5	3	-1	1	-1	0	3	1	0
Γ_6	2	0	$\sqrt{2}$	0	1	-2	$-\sqrt{2}$	-1
Γ_7	2	0	$-\sqrt{2}$	0	1	-2	$\sqrt{2}$	-1
Γ_8	4	0	0	0	-1	-4	0	1

Table A.1: Character table of the double group of the point Γ in zinc-blend-type semiconductors. Adapted from [24].

Following atomic physics it is possible now to symmetrize the wavefunctions so that their symmetry properties reflect the ones of the system. In particular, with spin, the wave functions are eigenstates of the total momentum operator $\mathbf{j} = \mathbf{l} + \mathbf{s}$ and therefore can be expressed as linear combinations of the eigenfunctions of the orbital angular momentum and spin giving rise to 6 states (tab.A.2).

The four-fold degenerate $j=3/2$ states belong to the Γ_8 representation since from tab.A.1 this is the only four-dimensional representation while the $j=1/2$ states belong to the Γ_7 representation. These two states are split by the spin-orbit coupling Δ_0 . The conduction

HH	$ \frac{3}{2} \frac{3}{2}\rangle$	$\frac{1}{\sqrt{2}} (X + iY) \uparrow\rangle$
	$ \frac{3}{2} -\frac{3}{2}\rangle$	$\frac{1}{\sqrt{2}} (X - iY) \downarrow\rangle$
LH	$ \frac{3}{2} \frac{1}{2}\rangle$	$\frac{1}{\sqrt{6}} (X + iY) \downarrow\rangle - \sqrt{\frac{2}{3}} Z \uparrow\rangle$
	$ \frac{3}{2} -\frac{1}{2}\rangle$	$-\frac{1}{\sqrt{6}} (X - iY) \uparrow\rangle - \sqrt{\frac{2}{3}} Z \downarrow\rangle$
SO	$ \frac{1}{2} \frac{1}{2}\rangle$	$\frac{1}{\sqrt{3}} (X + iY) \downarrow\rangle + \frac{1}{\sqrt{3}} Z \uparrow\rangle$
	$ \frac{1}{2} -\frac{1}{2}\rangle$	$-\frac{1}{\sqrt{3}} (X - iY) \uparrow\rangle + \frac{1}{\sqrt{3}} Z \downarrow\rangle$

Table A.2: $|j, m_j\rangle$ valence states. Adapted from[25].

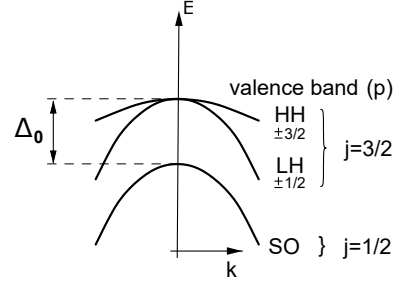


Figure A.1: III-V semiconductor's valence bands. Adapted from[26].

band belongs instead to Γ_6 .

The Bloch functions can be expanded in terms of band edge functions[27]

$$u_n(\mathbf{k}) = \sum_m c_m(\mathbf{k})u_{m\mathbf{0}} \quad (\text{A.5})$$

Inserting in eq.A.3, multiplying by $u_{n\mathbf{0}}^*$ and integrating over a unit cell a system of coupled equations with dimension given by the number of considered band edges in the expansion is obtained. For example, considering the coupling between the 6 Γ_{4v} , the 2 Γ_{6c} and the 6 Γ_{4v} bands (and not considering spin, T_d point group notation) results in a 14×14 determinant that has to be diagonalized.

In order to calculate analytically this determinant, *Löwdin* (quasi-degenerate) perturbation theory can be used (see for example [26]). Nevertheless, in this work a numerically approach is adopted as described in section A.2.

A.2 Superlattice

An 18x18 $\mathbf{k}\cdot\mathbf{p}$ model[28] has been adopted to simulate superlattice band structures. The approach is divided in two steps:

- 18x18 $\mathbf{k}\cdot\mathbf{p}$ bulk simulation of the constituents: there are 9 parameters: 4 coupling terms $P^2, (P')^2, Q^2, R^2$ and the 6 edge energies $\Gamma_{6c}, \Gamma_{7v}, \Gamma_{8v}, \Gamma_{7c}, \Gamma_{8c}, \Gamma_{3c}$ of which one is taken as reference so that there are actually 5 (see fig.A.2.). In the case of strain, Bir-Pikus model based on deformation potentials is employed[25]. Remember that strain causes a modification of the bulk energy edges.
- *envelope function approximation* in the superlattice. For superlattices, inputs of the model are the band offsets and bulk energy edges and gaps at Γ . Unstrained band offsets are taken from literature and then corrected through the Bir-Pikus model in case of strain as described in the previous point.

Envelope function approximation When a perturbation is introduced in a perfect crystal, like a quantum well or a superlattice, the wavefunction is no more given by the Bloch theorem but it is the product of a Bloch function $u_{n\mathbf{k}_0}$ and an envelope function,

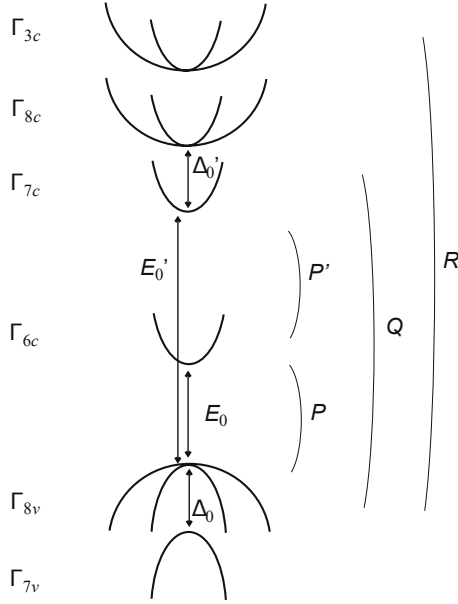


Figure A.2: 18×18 $\mathbf{k} \cdot \mathbf{p}$ model. Graphical representation of the involved input parameters. Adapted from [25].

slowly varying with respect to the Bloch function [20].

Considering an abrupt interface between two materials, according to the envelope function approximation, the wavefunction in layer A(B) for the miniband n can be written as[27]:

$$\Psi_{n\mathbf{k}}(\mathbf{r}) = \sum_i f_{i,n}^{A(B)}(\mathbf{r}) u_{i\mathbf{k}_0}(\mathbf{r}) \quad (\text{A.6})$$

where the index i spans over a set of band edges.

Considering lattice matching, the system is translationally invariant in the direction perpendicular to the growth direction z and therefore \mathbf{k}_\perp is a good quantum number. Then:

$$f_{i,n}^{A(B)}(\mathbf{r}_\perp, z) = \frac{1}{\sqrt{S}} e^{i\mathbf{k}_\perp \cdot \mathbf{r}_\perp} \chi_{i,n}^{A(B)}(z) \quad (\text{A.7})$$

where $\chi_{i,n}^{A(B)}(z)$ is the *envelope function* in layer A(B) and S is the heterojunction surface. Looking at the asymptotic behaviour of the envelope, it must satisfy the Bloch theorem and this allows to expand the periodic part of $\chi_{i,n}^{A(B)}(z)$ in a Fourier series:

$$\chi_{i,n}^{A(B)}(z) = e^{ik_z z} \sum_m a_n^{mi}(\mathbf{k}) e^{iG_m z} \quad (\text{A.8})$$

At the end:

$$\Psi_{n\mathbf{k}}(\mathbf{r}) = \sum_i \sum_m a_n^{mi}(\mathbf{k}) \frac{1}{\sqrt{S}} e^{i\mathbf{k}_\perp \cdot \mathbf{r}_\perp} e^{i(k_z + G_m)z} u_{i\mathbf{k}_0}(\mathbf{r}) \quad (\text{A.9})$$

where $G_m = \frac{2\pi}{d}m$, $\mathbf{k} = (\mathbf{k}_\perp, k_z)$ and $d = t_b + t_w$ is the superlattice period (t_b : barrier thickness, t_w : well thickness). Applying the superlattice Hamiltonian $H_{sl} = H_{bulk}^{A(B)} + V_{VB}(z)$, multiplying by $e^{-i(k_z + G_{m'})z} u_{j\mathbf{k}_0}^*(\mathbf{r})$ and integrating the problem becomes a $N \times N$ system of differential equations to be diagonalized. The dimension of the system is $N = 18 \times (2N_G + 1)$ where N_G is the number of G_m considered in the Fourier expansion ($N_G \leq m \leq N_G$). The numerically solved system is:

$$\sum_{m,m',i,j} a_n^{mi}(\mathbf{k}) \left\{ \frac{\hbar^2(\mathbf{k} + \mathbf{G}_m)^2}{2m_0} \delta_{m,m'} \delta_{i,j} + \frac{1}{d} \int_0^d e^{i(G_m - G_{m'})z} [\epsilon_i(z) + V_{VB}(z)] dz \delta_{i,j} + \frac{\hbar}{m_0} (\mathbf{k} + \mathbf{G}_m) \frac{1}{d} \int_0^d e^{i(G_m - G_{m'})z} \mathbf{P}_{ij}(z) dz \right\} = E_n(\mathbf{k}) a_n^{jm'}(\mathbf{k}) \quad (\text{A.10})$$

where $\epsilon_i(z)$ are the energy edges of the known (strained) bulk problem of the constituent materials, $V_{VB}(z)$ is the (unstrained) valence band edge variation along the growth direction (band offsets) and \mathbf{P}_{ij} is the matrix element between states i and j .

Bibliography

- [1] Baile Chen. *InP Based Type-II Quantum Wells PIN Photodiodes*. PhD thesis, University of Virginia, 2013.
- [2] Justin Easley, Christopher R Martin, Martin H Ettenberg, and Jamie Phillips. Ingaas/gaassb type-ii superlattices for short-wavelength infrared detection. *Journal of Electronic Materials*, 48(10):6025–6029, 2019.
- [3] Y Uliel, D Cohen-Elias, N Sicon, I Grimberg, N Snapi, Y Paltiel, and M Katz. Ingaas/gaassb type-ii superlattice based photodiodes for short wave infrared detection. *Infrared Physics & Technology*, 84:63–71, 2017.
- [4] David Z Ting, Alexander Soibel, and Sarath D Gunapala. Hole effective masses and subband splitting in type-ii superlattice infrared detectors. *Applied Physics Letters*, 108(18):183504, 2016.
- [5] David Z Ting, Alexander Soibel, Arezou Khoshakhlagh, Sam A Keo, B Rafol, Anita M Fisher, Brian J Pepper, Edward M Luong, Cory J Hill, and Sarath D Gunapala. Advances in iii-v semiconductor infrared absorbers and detectors. *Infrared Physics & Technology*, 97:210–216, 2019.
- [6] GA Sai-Halasz, R Tsu, and L Esaki. A new semiconductor superlattice. *Applied Physics Letters*, 30(12):651–653, 1977.
- [7] Yaojiang Chen, Zhiyang Xie, Jian Huang, Zhuo Deng, and Baile Chen. Two-micron wavelength high speed photodiode with ingaas/gaassb type-ii multiple quantum wells absorber. *arXiv preprint arXiv:1905.07258*, 2019.
- [8] Giovanni Ghione. *Semiconductor devices for high-speed optoelectronics*, volume 116. Cambridge University Press Cambridge, 2009.
- [9] Federico Capasso, Khalid Mohammed, and Alfred Y Cho. Resonant tunneling through double barriers, perpendicular quantum transport phenomena in superlattices, and their device applications. In *Electronic Structure of Semiconductor Heterojunctions*, pages 99–115. Springer, 1988.
- [10] R Tsu and Leo Esaki. Tunneling in a finite superlattice. *Applied Physics Letters*, 22(11):562–564, 1973.
- [11] L_L Chang, Leo Esaki, and R Tsu. Resonant tunneling in semiconductor double barriers. *Applied Physics Letters*, 24(12):593–595, 1974.

- [12] B Ricco and M Ya Azbel. Physics of resonant tunneling. the one-dimensional double-barrier case. *Physical Review B*, 29(4):1970, 1984.
- [13] Holger T Grahn. *Semiconductor superlattices: growth and electronic properties*. World Scientific, 1995.
- [14] Leo Esaki and Ray Tsu. Superlattice and negative differential conductivity in semiconductors. *IBM Journal of Research and Development*, 14(1):61–65, 1970.
- [15] Vassil Palankovski. *Simulation of Heterojunction Bipolar Transistors*. PhD thesis, The Vienna University of Technology, 2000. URL <https://www.iue.tuwien.ac.at/phd/palankovski/diss.html>. Sec. 3.6.2.2.
- [16] D Calecki, JF Palmier, and A Chomette. Hopping conduction in multiquantum well structures. *Journal of Physics C: Solid State Physics*, 17(28):5017, 1984.
- [17] H Schneider and K v Klitzing. Thermionic emission and gaussian transport of holes in a gaas/al x ga 1- x as multiple-quantum-well structure. *Physical Review B*, 38(9):6160, 1988.
- [18] David Z Ting, Alexander Soibel, and Sarath D Gunapala. Type-ii superlattice hole effective masses. *Infrared Physics & Technology*, 84:102–106, 2017.
- [19] David ZY Ting, Alexander Soibel, Linda Höglund, Jean Nguyen, Cory J Hill, Arezou Khoshakhlagh, and Sarath D Gunapala. Type-ii superlattice infrared detectors. In *Semiconductors and Semimetals*, volume 84, pages 1–57. Elsevier, 2011.
- [20] John H Davies. *The physics of low-dimensional semiconductors: an introduction*. Cambridge university press, 1998.
- [21] S.M. Sze and K.K. Ng. *Physics of Semiconductor Devices*. Wiley, 2006. ISBN 9780470068304.
- [22] A. Rogalski. *Infrared and Terahertz Detectors*. CRC Press, Taylor & Francis Group, 2018. ISBN 9781138198005.
- [23] I. Vurgaftman, J. R. Meyer, and L. R. Ram-Mohan. Band parameters for iii–v compound semiconductors and their alloys. *Journal of Applied Physics*, 89(11):5815–5875, 2001. doi: 10.1063/1.1368156.
- [24] P. YU and M. Cardona. *Fundamentals of Semiconductors: Physics and Materials Properties*. Graduate Texts in Physics. Springer Berlin Heidelberg, 2010. ISBN 9783642007101.
- [25] Morten Willatzen, Lew Yan Voon, and C Lok. *The kp Method: Electronic Properties of Semiconductors*. Springer, 2009.
- [26] R. Winkler. *Spin-orbit Coupling Effects in Two-Dimensional Electron and Hole Systems*. Springer Tracts in Modern Physics. Springer Berlin Heidelberg, 2003. ISBN 9783540011873.

BIBLIOGRAPHY

- [27] G. Bastard. *Wave mechanics applied to semiconductor heterostructures*. Monographies de physique. Les Éditions de Physique, 1988. ISBN 9780470217085.
- [28] B Vinter. Auger recombination in narrow-gap semiconductor superlattices. *Physical Review B*, 66(4):045324, 2002.